Comprehensive Study of Oxygen Storage in YbFe2O4+x ($x \leq 0.5$): Unprecedented Coexistence of FeOn Polyhedra in One Single Phase

Sarah Nicoud, Marielle Huvé, Olivier J. Hernandez, Alain Pautrat, Mathieu Duttine, Alain Wattiaux, Claire Colin, Houria Kabbour, Olivier Mentré

A comprehensive study of oxygen storage in $YbFe_2O_{4+x}$ ($x \leq 0.5$): unprecedented coexistence of FeO_n polyhedra in one single phase

Sarah Nicoud[1], Marielle Huvé[1], Olivier Hernandez[2], Alain Pautrat[3], Mathieu Duttine[4], Alain Wattiaux[4], Claire Colin[5], Houria Kabbour[1], Olivier Mentré[*,1]

[1] Univ. Lille, CNRS, Centrale Lille, ENSCL, Univ. Artois, UMR 8181 - UCCS - Unité de Catalyse et Chimie du Solide, F-59000 Lille, France
[2] ISCR, UMR CNRS 6226 -Université de Rennes 1, F-35042 Rennes, France
[3] CRISMAT, UMR 6508-CNRS, ENSICAEN, Caen, France
[4] CNRS, Univ. Bordeaux, ICMCB, UPR 9048, F-33600 Pessac, France
[5] Université Grenoble Alpes, Institut NEEL, F-38000 Grenoble, France

* Corresponding author, email Olivier.mentre@ensc-lille.fr

Abstract:

The multiferroic $LuFe^{2.5+}{}_2O_4$ was recently proposed as a promising material for oxygen storage due to its easy reversible oxidation into $LuFe^{3+}{}_2O_{4.5}$. We have investigated the similar scenario in $YbFe_2O_{4+x}$ leading to a slightly greater oxygen storage capacity (OSC) of 1434 µmol O/g. For the first time, the structural model of $LnFe_2O_{4.5}$ was fully understood by high resolution microscopy images, synchrotron & neutron diffraction experiments as well as maximum entropy method. The oxygen uptake promotes a reconstructive shearing of the [YbO_2] sub-units controlled by the adaptive Ln/Fe oxygen coordination and the $Fe^{2/3+}$redox. After oxidation, the rearrangement of the Fe coordination polyhedra is unique such that all available FeO_n units (n = 6,5,4 in octahedra, square pyramids, trigonal bipyramids, tetrahedra) were identified in modulated rows growing in plane. This complex pseudo-ordering gives rise to short range antiferromagnetic correlation within an insulating state.

1) Introduction

The chemistry of multiferroic materials has become one of the hottest discipline of materials science in the beginning of the 21st century. Particularly two distinct series of inorganic materials have emerged with original mechanisms involved for their multiferroicity (MF), i.e. the layered rare-earth manganites $RMnO_3$ (R=Y, Sc, In, Ho...Lu) and layered rare-earth ferrites RFe_2O_4 (R = Y, In, Ho…Lu).[1] A strong structural analogy exists between their crystal structures, due to the common CdI_2-like $_\infty[RO_2]$ layers sandwiched between either simple ($RMnO_3$ case) or double (RFe_2O_4 case) layers of trigonal bipyramids (TBP).[2] Given this structural resemblance, the labile anionic stoichiometry reported in both types leads to a fascinating chemical playground to generate novel polymorphs with new emerging properties at the frontier between magnetoelectrics and ionic conductors. Factually in both series, upon oxidation/reduction cycles, a significant amount of oxygen interstitials/vacancies participate to the reversible topotactic restacking between structural modules.

For instance, besides the reduction of $YMn^{3+}O_3$ into $YMn^{2/3+}O_{3-x}$ intermediates using hydride reactants [3], we have recently evidenced a reconstructive and reversible reduction into $YMn^{2+}O_2$ [4], after ammonolysis treatment. The structural rearrangement is drastic, leading to an original disordered composite structure between $_\infty[YMn^{2+}O_{2+x}]^{(1-2x)+}$ and $_\infty[YMn^{2+}O_{3-x}]^{(1+2x)-}$ blocks with a mixture of various $Mn^{2+}O_n$ coordinations. By comparison, less drastic oxygen sub-stoichiometry was reported in the RFe_2O_4 ferrites.[5] Upon oxidation, both $RMnO_3$ and RFe_2O_4 are known to admit a significant amount of interstitial anions in their TBP-based layers although the structural mechanisms is far to be understood despite a large number of studies. In $(Y,Dy)MnO_{3+x}$, a *x* value up to *ca.* 0.3 was reported under oxygen pressure, and preliminary structural hypotheses have been proposed by means of powder neutron diffraction (PND) but remains still not elucidated. At least a position of the interstitial oxygen sites was proposed but too close from the original anions.[6] In the oxidized RFe_2O_{4+x} materials the structural aspect is expected all the more puzzling, due to the number of phenomena which coexist in the crystals, and depend on the x value and on the R chemical nature[7–9]: i) Modulated Fe^{2+}/Fe^{3+} charge ordering (CO) for low x values. Reported COs are various and expend in limited domains. They stand at the origin of the RFe_2O_{4+x} multiferroicity due to the creation of charge ordered ferroelectric or antiferroelectric domains.[10] In the case of $LuFe_2O_{4+x}$, at least three independent commensurate or incommensurate CO modulations (called q_2, q_3, q_4 in the literature) have been identified below T_{CO} =330 K.[11,12] ii) Independently, large modulated areas are assigned to specific O_{4+x} oxygen segregation and/or modulated Lu displacements.[11] More recently, it was shown that the strongly hyperstoichiometric oxidized compounds (i.e. after the $LuFe^{2.5+}{}_2O_4 \rightarrow LuFe^{3+}{}_2O_{4.5}$ oxidation), shows a non-elucidated topotactic rearrangement between the cationic layers. Here

again a number of intermediate $LuFe^{2/3+}_2O_{4.5-x}$ polytypes have been identified on the basis of their

electron diffraction (ED) patterns which show new sets of modulated satellites which seem to depend on x.[12,13] In this mysterious $LuFe_2O_{4.5}$ oxidized form, such aperiodic phenomena coherent within relatively small domains and complex twinning effects complicate the real-space crystallographic vision. Clearly no refined structural model was proposed so far for the latter compound and the location and arrangement of interstitial oxygen in the dense double layers remains unknown at the moment while this structural feature is obviously of upmost importance.

The connection between both cationic and anionic subarrays of the stoichiometric (O_4) and hyperstoichiometric ($O_{4.5}$) materials is still unclear while directly connected to the oxygen storage properties.[13] Note that all abovementioned modulations show a component perpendicular to the *c*-stacking (across the $_\infty[LuO_2]$ spacers) which involves an ideal 3D ordering that we aim to characterize. This gap in the literature is a promising avenue of research to be explored, particularly for R = Yb, not yet investigated for its redox abilities. However the mixed valence pristine compound shows similar multiferroic properties as its Lu-analog due to polar charge-ordered domains with magnetic frustration.[14,15]

The offered multifunctional potentialities in such labile layered mixed valence $Fe^{2/3+}$ oxides is enormous for tuning magneto-electric couplings but also in solid-state ionic devices for oxygen storage, sensors or energy conversion.[16,17,18] Here we report a comprehensive study of the transformation of $YbFe_2O_4$ into $YbFe_2O_{4.5}$ based on atomistic structural models refined from the combined use of synchrotron and neutron diffraction techniques at the average and modulated level.

In a primary stage, we revisited the structure of the $YbFe_2O_{4.0}$ precursor compound, with regard to the existing literature to better characterize the anionic subarray by means of PND. After oxidation, the unprecedented distribution of all available $Fe^{3+}O_n$ units with n = 4 (tetrahedra), 5 (TBP, square pyramids), 6 (octahedra) in $YbFe_2O_{4.5}$ is for the first time evidenced as a key structural feature opening new perspectives for the design and characterization of promising coupled magnetoelectrics and ionics materials. The evolution of their electric and magnetic properties are explained on the basis of the structural changes.

2) Experimental techniques

Synthesis: The $YbFe_2O_4$ phase was prepared using stoichiometric mixtures of Yb_2O_3, Fe_2O_3 and Fe powders with the ratio 1/2:5/6:1/3. The mixture was finely ground and pressed into pellets, then placed into an evacuated silica tube heated at 1000°C for 36 hours and quenched at room temperature. The subsequent product was oxidized at 600°C in air for 6 hours. The final product corresponding to the phase $YbFe_2O_{4.5}$ exhibits a dark brown color. Note that depending on the prepared samples, $YbFe_2O_4$ may be accompanied by a minor amount of orthorhombic-perovskite

$YbFeO_3$ impurity, revealed in PND or synchrotron-XRD patterns, but not observed by standard laboratory XRD.

XRD: the XRD powder pattern of the samples was collected on a Bruker D8 diffractometer equipped with a linear detector Lynxeye (Cu K_α) in Bragg-Brentano geometry. The pattern was measured in the 2θ range 5°-80° (with a step of 0.02°) at room temperature.

High temperature X-ray diffraction: the high temperature study was performed using a Bruker D8 equipped with XRK900 chamber under flowing air or H_2/N_2 (3%) atmosphere from room temperature to 600°C.

Synchrotron: synchrotron X-ray powder diffraction data were collected at Argonne National Laboratory (U.S.A.). The measurement was performed on the 11-BM beamline using λ= 0.414179 Å in the 2θ range 0.5°-50°.

Powder Neutron Diffraction (PND): experiments were carried out on the D1B beamline of the ILL (Institute Laue Langevin, France) using λ=1.28 Å in the 2θ range 0.8°-129°. The PND based refinements of the modulated $YbFe_2O_{4.5}$ phase and of the non-modulated $YbFe_2O_4$ phase were performed using the program JANA 2006.[19] FULLPROF [20] was used as well to refine the $YbFe_2O_{4.5}$ structure from synchrotron data.

Maximum Entropy Method: MEM electronic or nuclear densities maps have been computed with the PRIMA program [21] using *F*-constraints, uniform prior densities and the 0^{th} order single-pixel approximation mode. The observed structure factors were extracted according to Rietveld refinements against powder data (considering an average structural model in the case of the modulated $YbFe_2O_{4.5}$ material) carried out with the Rietan-FP program [22] using a split pseudo-Voigt profile function.

Thermogravimetric Analysis: the TG analysis was performed on a Sestys Evolution Setaram device. The sample evolution was measured from room temperature to 700°C at 5°C/min under air flow.

TEM: Electron diffraction patterns and HRTEM images were obtained on a FEI Technai G2-20 twin TEM microscope. HAADF images were acquired on a TEM FEI TITAN Themis 300. It is equipped with a probe corrector for resolution of 0.7 Å in STEM mode. The powder was crushed and the alcoholic suspension deposited on carbon supported copper grids followed by evaporation under ambient condition.

Mössbauer spectroscopy: ^{57}Fe Mössbauer measurements were performed using a constant acceleration Halder-type spectrometer operating in transmission geometry with a room temperature ^{57}Co source (Rh matrix). The velocity scale was calibrated according to the ^{57}Fe Mössbauer spectrum

of a pure α-Fe^0 foil recorded at room temperature. The polycrystalline absorbers were prepared in

order to contain about 10 mg/cm^2 of iron and thus, to avoid saturation effects. The refinement of Mössbauer hyperfine parameters (δ isomer shift, Δ quadrupole splitting, Γ signal linewidth and relative areas) was performed using both homemade programs and the WinNormos software.[23] Distributions of hyperfine parameters (quadrupole splitting or hyperfine magnetic field) have been considered for overlapped components presenting apparent linewidth higher than 0.35 mm/s, following the method described by Hesse and Rübartsch. [24]

3) Fine characterization of the $YbFe_2O_{4.0}$ precursor

Keeping in mind our motivations and issues, one should in a preliminary stage revisit the crystal chemistry of the pristine $YbFe_2O_4$ phase. Intensive studies were carried out on the nanometric charge-ordered domains in $YbFe_2O_4$ [14,15] giving rise to controversial T_{CO} values. For instance charge-ordered domains in a nanometer scale were observed below 353 K by electron microscopy [14] while a passage from 3D to 2D CO was estimated at *ca.* 300 K from high temperature Raman spectroscopy. [25] In contrast, to the best of our knowledge no PND analysis was reported for a fine description of the parent anionic subarray, a necessary task in prevision of its oxygen incorporation. For subtle nuances, our crystallographic work was assisted by MEM calculations as a way to get most probable model-free atomic densities (quite independent from the parametric Rietveld refinements).

3.1 Oxygen stoichiometry and cationic off-centering: The reported $YbFe_2O_4$ crystal structure (space group $R3m$) is shown figure 1a. Dealing with the cation-containing layers, it corresponds to a [ABA][BCB][CAC] stacking type between next [Y],[FeO],[FeO] layers, Fig. 1b. Contrarily to the fine monoclinic distortion reported for $LuFe_2O_4$ below T_{CO} = 330 K [7,11], similar split was never reported for $YbFe_2O_4$ nor in our well resolved pattern using a pure Kα1 radiation, such that our PND Rietveld refinement was conducted in the trigonal $R3m$ space group. All atoms were refined anisotropically as shown figure 2a,b leading to *x* =0.0 value (R_{Bragg} = 1.99 %). Indeed the Fourier difference maps did not show any evidence of interstitial sites, as confirmed by the Maximum Entropy Method (MEM) discussed later (see Fig. 6a). All anisotropic displacement ellipsoids show reasonable values except that of the Yb site strongly elongated along the *c*-axis (U_{33} = 48xU_{11}). It reflects a strong off-centering of Yb atoms as shown below by TEM, similar to the Lu-wave observed for $LuFe_2O_{4+x}$ with x ~0.[12] Crystallographic parameters and selected bond distances are listed in the Table 1 and supplementary information S1a-c. As prepared $YbFe_2O_4$ is very stable at room temperature in air, as shown by similar lattice parameters refined six month after synthesis, see suppl. information S1.

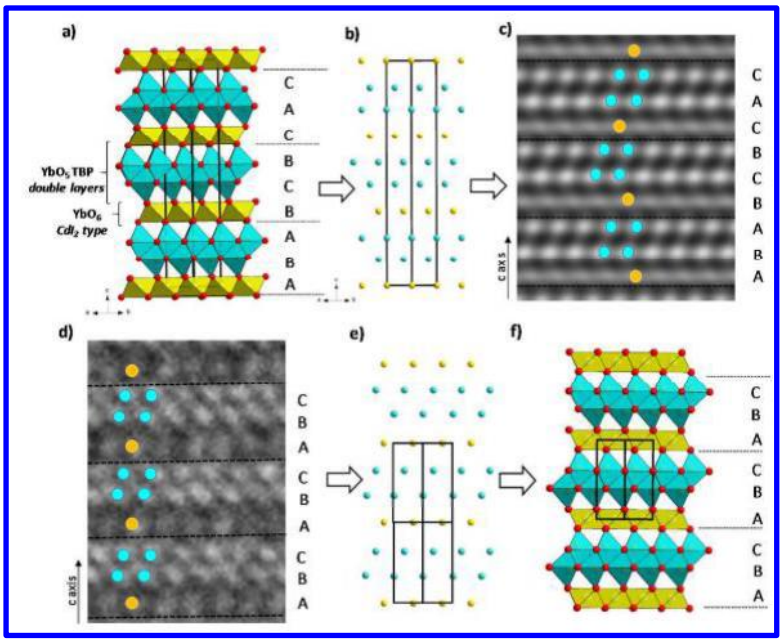

Figure 1: *Structure of $YbFe_2O_4$ and deduction of the average $YbFe_2O_{4.5}$ crystal structure: a,b) The crystal structure of $YbFe_2O_4$ and its cationic packing. c) Matching with the [010] simulated HREM image for defocus and thickness values Δf= 0 Å, Δt= 24.2 Å. d) $YbFe_2O_{4.5}$: the [010] experimental HREM image. e,f) Deduced cationic packing and structural model.*

Table 1 : atomic coordinates and displacement parameters for $YbFe_2O_4$ at RT from PND data (space group R-3m, a=3.43522(6) Å, c=24.9751(6) Å, R_{Bragg} = 1.99%,

Atom,site	x	y	Z	U_{eq}	$U_{11}=U_{22}$	U_{33}	U_{12}	$U_{13}=U_{23}$
Yb, *3a*	0	0	0	0.0132	0.0008(8)	0.038(1)	0.0004(8)	0
Fe, *6c*	0	0	0.21531(7)	0.0083	0.0095(8)	0.0060(9)	0.0047(8)	0
O1, *6c*	0	0	0.2925(1)	0.0075	0.008(1)	0.008(1)	0.004(1)	0
O2,*6c*	0	0	0.1278(1)	0.0222	0.020(1)	0.027(2)	0.010(1)	0

3.2 Additional modulated features at the microscopic scale: Our refined crystallographic model does not reflect microscopic phenomena relative to Fe^{2+}/Fe^{3+} CO domains mentioned above. However our electron microscope study reveals diffraction satellites typical of the CO phenomena (q_{-2}, q_{-3}) and of other structural specificities (q_{-1}) explained and labelled on the basis of the abundant literature on RFe_2O_4 compounds (R=Lu, Yb). Before oxidation, selected-area electron diffraction (SAED along the $[-110]_R$ zone-axis direction) for $YbFe_2O_4$ at room temperature is shown Figure 2c, where the R indice refers to the rhombohedral setting. It shows the characteristic diffuse streaks along *h*/3, *h*/3, *l* lines (corresponding to $q_{-2,YbFe2O4}$) assigned to short range CO effects.[14] According to the literature it corresponds to CO correlation length from 3 to 7 nm in-plane, while the domain thickness along the *c* axis is even smaller. For comparison, in $LuFe_2O_4$, those diffuse lines include dots

assigned to the so-called $q_{1,LuFe_2O_4}$ and $q_{1,LuFe_2O_4}$ modulation spots which vanish above T_{CO} = 330 K.[11,12]

Compared to the satellites of CO origin, in all tested samples, the $[010]_R$ zone axis pattern (ZAP) shows more intense modulated spots, which correspond to $q_{1,YbFe2O4}$ = ~0.28 a_R^* + ~1 c_R^* (fig. 2d) and that are absent in the $[100]_R$ ZAP (fig. 2e). It is assigned in $LuFe_2O_{4+x}$ to tiny oxygen over-stoichiometry /segregation together with Lu displacive wave in large domains[11,12] (few hundred of nanometers). The Yb displacement wave is shown on high resolution images, see figure 2f, and occurs although no oxygen over-stoichiometry was detected by PND. It forms undulated rows growing along the *a*-axis, absent along *b*, which formally break the rhombohedral symmetry and are assigned to the $q_{1,YbFe2O4}$ modulation vector. We did not find evidences of the corresponding satellites in our high resolution XRD nor PND data which comfort short-range non-cooperative displacements. $q_{1,YbFe2O4}$ ([010] ZAP) and $q_{2,YbFe2O4}$ ([-110]$_R$ ZAP) are observed on two distinct reciprocal planes rotated by 30° around c* in the same crystallites by tilting. After oxidation, one expects the vanishing of all CO related phenomena in $YbFe^{3+}{}_2O_{4.5}$.

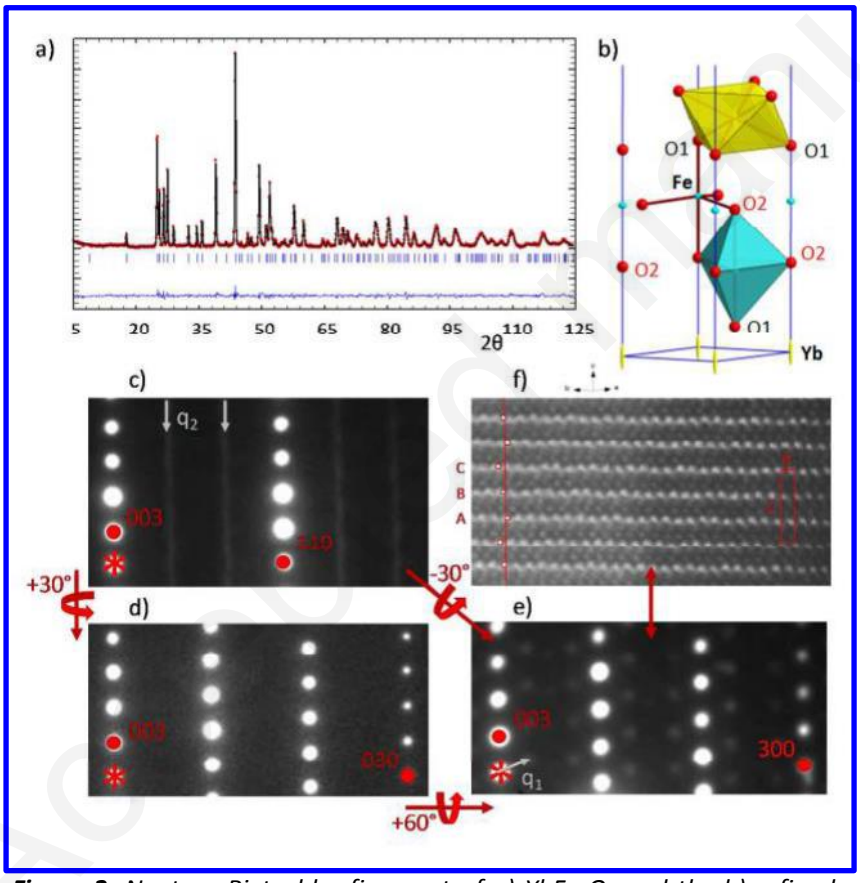

Figure 2: *Neutron Rietveld refinement of a) $YbFe_2O_4$ and the b) refined crystal structure. Electron diffraction Zone Axis Patterns of $YbFe_2O_4$: c) [-110] with arrows pointing q_2 (CO) streaks. d) [100] e) [010] with arrows showing 1st?? f) HREM image corresponding to e) with undulated Yb rows along the a-axis in agreement with the anisotropic displacements of the Yb site of b).*

3.3 Fe^{2+} / Fe^{3+} charge partitioning: In the stoichiometric compound, one should give a special attention to the Fe ions spectral features for comparison purpose after oxidation. In this goal, ^{57}Fe

Mössbauer gives important insights about the local and collective Fe^{2+} vs Fe^{3+} interplay in $YbFe_2O_{4.0}$. Unsatisfactory attempts to reconstruct the room temperature ^{57}Fe Mössbauer spectrum with two or three discrete quadrupole doublets (with Lorentzian lineshape) actually led us to consider three components, one quadrupole doublet and two distributions of quadrupole doublets which reflect local heterogeneity due in part to the Yb off-centering discussed above, see Figure 3 and section S3e. Each distribution corresponds to the sum of discrete quadrupole doublets with Lorentzian lineshape (linewidth: 0.30 mm/s from a α-Fe0 reference), same isomer shift but different quadrupole splitting values. We note that this splitting affects essentially Fe^{2+} (d^6) species due to their largest contribution of 3d electron to the total electric field. It validates the Fe^{2+}:Fe^{3+} ratio of 1:1 as follows. The hyperfine parameters reported in Table 2, isomer shift and quadrupole splitting values, are characteristic of five-fold TBP iron ions coordination.[26] The three components correspond to Fe^{3+} (δ=0.31 mm/s, relative area 39%), Fe^{2+} (δ=0.91 mm/s, relative area 41%) and intermediate valence iron $Fe^{2/3+}$ (δ=0.51 mm/s, relative area 20%) unresolved due to fast electronic transfer. In the latter, the Fe^{2+} *vs.* Fe^{3+} contribution was determined considering a linear evolution of the isomer shift value [27] from 0.31 mm/s (Fe^{3+}) to 0.91 mm/s (Fe^{2+}). We find for the $Fe^{2/3+}$ contribution 7% Fe^{2+} and 13% Fe^{3+}leading to the mean 48% (Fe^{2+}): 52% (Fe^{3+}) relative contributions to the Mössbauer spectrum as expected from the $YbFe^{2.5+}O_4$ formula. Finally it validates the co-presence of both localized Fe^{2+}/Fe^{3+} CO (*ca* 80%) and delocalized mixed $Fe^{2/3+}$ nano-domains (*ca.* 20%) from our ED study and allows anticipating the semiconductive regime further discussed.

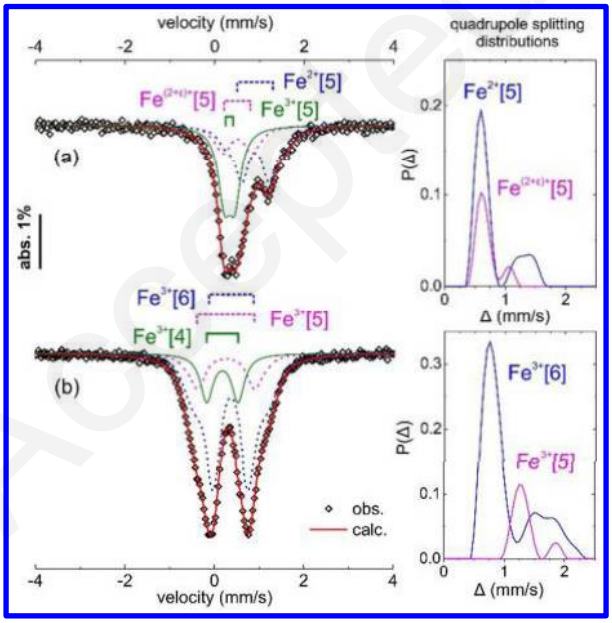

Figure 3: *Room temperature ^{57}Fe Mössbauer spectrum of a) $YbFe_2O_4$ and b) $YbFe_2O_{4.5}$: The components with dashed lines were calculated considering a distribution of the quadrupole splitting parameter.*

*Table 2: ^{57}Fe Mössbauer hyperfine parameters determined from the fitting of $YbFe_2O_4$ and $YbFe_2O_{4.5}$ spectrum (Figure 3). Isomer shift values are expressed with respect to α-Fe at room temperature. *mean value of the quadrupole splitting distribution.*

	δ (mm/s)	Δ (mm/s)	Γ (mm/s)	Area (%)
$YbFe_2O_4$				
Fe^{3+} [5]	0.31(2)	0.24(3)	0.33(3)	39(2)
$Fe^{(2+\varepsilon)+}$ [5]	0.51(5)	0.59*	0.30(-)	20(2)
Fe^{2+} [5]	0.91(2)	0.79*	0.30(-)	41(2)
$YbFe_2O_{4.5}$				
Fe^{3+} [4]	0.17(3)	0.70(3)	0.34(2)	16(4)
Fe^{3+} [5]	0.25(3)	1.34*	0.30(-)	18(4)
Fe^{3+} [6]	0.36(2)	1.04*	0.30(-)	66(5)

4) Transformation into the hyperstoichiometric $YbFe_2O_{4.5}$

4.1 State of the art : The oxidation of layered ferrite was first given scientific consideration in the 80's by Gerardin *et al.*, when they published the discovery of a series of lanthanide-based oxides announced as $RFe_2O_{4.5}$ after heating in air RFe_2O_4 precursors (R=Lu, Yb, Tm, Er, Ho, Y, In).[28] However, no crystallographic data for these compounds exists apart from the determination of its primitive trigonal symmetry related to the pristine compound as follows : $a_{YbFe2O4.5} = a_{YbFe2O4}$; $c_{YbFe2O4.5} = 1/3\ c_{YbFe2O4}$.

In 2013, Hervieu *et al.* conducted the relevant investigation of the transformation of $LuFe_2O_4$ into $LuFe_2O_{4+\delta}$, where δ ranged between 0 and 0.5.[12,13] The oxidation up to $LuFe_2O_{4.5}$ was shown to occur progressively, without distinct boundaries between metastable intermediate steps, from TGA and XRD analyzes. The onset of oxygen intercalation started at reasonably low temperatures (≈200°C), which is significant for oxygen storage application. However, once again, no positional crystallographic information concerning the intercalated oxygen was proposed.

4.2 Low thermal activation and reversibility: The oxidation of $YbFe_2O_4$ was achieved by treating the prepared precursor materials to temperatures around 600°C under air and was further monitored by TGA (see Fig.4a,b) and in-situ HTXRD pattern (see fig.4c,d). The TGA (rate 5°C/min) shows a continuous mass uptake above *ca.* 200°C until a flat plateau above 380°C. The final oxidized form is stable upon cooling in air. The gain of 2.22% leads to the final formula $YbFe_2O_{4.48}$ in good agreement with the ideal $YbFe^{3+}O_{4.5}$ formula. Figure 4b shows the TGA plot in air until 225°C (5°C/min) followed by an isotherm for 180 min. After initialization of the oxidation wave, the mass uptake is pursued until x=0.5. This result reveals an oxidation process under kinetic rather than thermodynamic control.

It validates that all possible $YbFe_2O_{4+x}$ intermediates (x<0.5) are metastable phases. Similarly, in $LuFe_2O_{4+x}$ the oxidation was continued during isothermal steps.[13] The high temperature XRD of $YbFe_2O_4$ was conducted under air (heating, 50°C/min) and then under 3% H_2/N_2 gas (heating, 50°C/min) to probe the reversibility. The high temperature XRD patterns are provided in Suppl. information S2. On heating, noticeable changes in the patterns appear around 250°C. In the range of the next 100°C, a mixture of phases is present, and then peaks shift in accordance with the evolution of the lattice from $YbFe_2O_4$ to $YbFe_2O_{4.5}$, continuously through metastable intermediates. It comforts the trigonal cell originally reported. [28] The evolution of the reduced cell parameters during oxidation is shown figure 4c and validates a main lattice dilatation after oxidation. It is significant that no residual $YbFe_2O_4$ is present, indicating that full oxidation took place. Note that above 700°C the resulting product is indeed $YbFe_2O_{4.5}$, albeit with some evidence of decomposition impurities Yb_2O_3 and Fe_2O_3. Under 3% H_2/N_2, the back-transformation of $YbFe_2O_{4.5}$ occurs at 450°C in our experimental conditions, as shown figure 4d and leads to $YbFe_2O_4$ single-phase. We note that a rapid STEM examination just after treatment barely shows the CO diffuse lines ($q_{1.2,YbFe2O4}$) with strongly weakened intensity, while $q_{1.1,YbFe2O4}$ is absent which reveals a metastable exact $Fe^{2.5+}$ state with even smallest CO domains, and no Yb displacive correlations compared to the as-prepared pristine phase.

4.3 High oxygen storage capacity (OSC): The oxygen uptake (air) and release (H_2/N_2) occurring at very similar temperature that for $LuFe_2O_4$ [12,13]one assume similar aptitudes on cycling and attractive OSC , with somewhat improved values due to lighter Yb. We calculate 1426 (Yb) against 1414 (Lu) µ.mol O/g while the lutetium price is prohibitive. This OSC is far below those of particular oxides such as the 114 $YBa(Fe,Mn)_4O_{7+\delta}$ (OSC = *ca.* 4000 µ.mol /g) [29] or delafossite $CuMnO_2$-$nCeO_2$ composites [30] (OSC = ca. 3000 µmol /g) or oxysulfides Ln_2O_2S (OSC = ca. 8000 µ.mol /g) [31] which relies on the $Fe^{2/3+}$,Mn^{2+}/ Fe^{3+},$Mn^{3/4+}$, Cu^{+}/Cu^{2+} and S^{2-}/S^{6+} couples respectively, but with more convenient working temperature at least concerning the post-reduction, i.e. 400°C in 3% H_2/N_2. In that sense it is in the range of admitted working temperatures for oxygen storage in automotive catalysts (*ca.* 400°C) dominated by CeO_2 based compounds (Ce^{3+}/Ce^{4+} couple). [32]

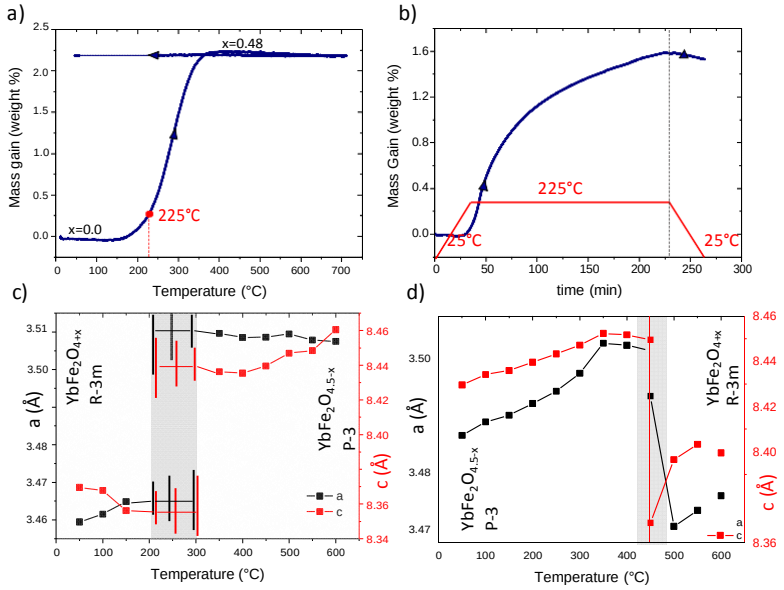

Figure 4: *Oxidation of $YbFe_2O_4$. TGA plots a) until 700°C under air flow. b) until 225°C followed by 225°C isotherm for 3 hours. c) In-situ reduced parameters (a and c in the P-centered trigonal cell; a and c/3 in the R-centered one) during oxidation and d) the reversible reduction in 3% H_2/N_2. The error bars in the dashed multiphasic areas denote strong inaccuracy.*

5) Unravelling the real crystal structure of hyperstoichiometric $YbFe_2O_{4.5}$

5.1 Average crystal structure: Here, our goal is to determine the $YbFe_2O_{4.5}$ average structural model and to locate /quantify the anionic subarray. It was initially determined on the basis of the HREM phase contrasts images. Our main strategy is depicted in Figure 1 and involves a decoding of the experimental [010] image, using atomic contrasts calculated for the parent $YbFe_2O_4$ phase according to the [ABA][BCB][CAC] stacking sequence (R3m space group) described above, fig 1a-c. By comparison $YbFe_2O_{4.5}$ shows a [ABC] stacking type in a primitive trigonal cell, fig.1d-f similarly to what observed for $LuFe_2O_{4.5}$ [12,13]. However no structural refinement was provided leading to a blank field about the "ideal" atomic coordinates and average symmetry. To fill the gap, one could create by hand, a model matching the HREM image. The most symmetric space group is P3 for a consistent crystal structure with pertinent interatomic distances. Of course at this stage no information is available about the location of the interstitial oxygen anions.

The deduced average model was refined using both synchrotron XRD and PND data. The sample used at the synchrotron contained well crystallized $YbFeO_3$ perovskite (w% = 2.62(2)). Dealing with the synchrotron data, the P3 symmetry was used and only weak asymmetric broadening of some peaks was observed due to stacking faults described in the next section. On cooling, apart from a slight cell contraction no evidence of any peak splitting was detected which validates the trigonality of the

average unit cell, see suppl. Information S3a. We obtained at 295 K a= 3.481064(9) Å, c =8.42915(4) Å$_{synchr.}$ and at 100 K a= 3.476689(8) Å, c =8.42122(3)Å$_{synchr}$.

Interstitial oxygen atoms O_{int} have been located using both Fourier difference and maximum entropy method (MEM) maps, even found dealing with XRD data, see figure S4a. They appear on 2(d) sites (x=0, y=0, z=0.347(2)$_{PND}$/0.3364(4)$_{synchr.}$) leading to short O2-O_{int} "average" distances of 2.18$_{PND}$/2.06$_{synchr.}$ Å regardless of any modulation, see figure 5b. The local constraints due to the "push and pull" interplays lead to partial occupancies of O_2 (2(d); Occ. = 0.74(2)%) and O_{int} (2(c); Occ. = 0.51(2)%)$_{NPD}$, which have been refined while the O2+O_{int} occupancies are restrained for fulfilling a $YbFe_2O_{4.5}$ stoichiometry. At this stage, we note for the PND results, that the O2/O_{int} ratio depends on the modelling of the background. The combined refinement of the average crystal structure using both diffraction sources leads to a similar model with R_{Bragg} = 6.99 % $_{PND}$ and R_{Bragg} = 5.34 % $_{synchr}$. The atomic coordinates (PND) of the average model are given in Table 3. Details of the synchrotron fit are given in the supplementary material, S3b. Main results concerning the $YbFe_2O_{4.5}$ average structure are listed below:

- Immediately, the partial occupancy of O2 involves that a significant part of the initial TBP loses at least one apical corner leading to FeO_{4+n} tetrahedra or square pyramids, depending on the contribution of O_{int}. This point is crucial for understanding the real-space model detailed below.

- Yb and Fe anisotropic displacement parameters have been refined and show rather large contribution in the (a,b) plane and along c, in part reminiscent of the $YbFe_2O_4$ case, see figure 5f. Interestingly, in the hyperstoichiometric phase and with regard to their values in the stoichiometric phase, the root-mean-square (RMS) displacement (in Å) of the cations Yb remains almost unchanged along c, while along a/b they are increased by a factor of 7. Those results reveal that the huge disorder of Yb along c cannot be directly related with the oxygen uptake. We recall that, as no observable satellites were detected by PND for $YbFe_2O_{4.0}$, the huge anisotropic disorder experienced by the strong neutron scatterer Yb in the latter material is either statistics or short-to-medium range ordered. See details about RMS and MEM conclusions in supplementary S4. Similar arguments have to be kept in mind, dealing with Yb off-centering in $YbFe_2O_{4.5}$.

- After incorporation of 0.5 oxygen, the Yb site conserves its flattened octahedral coordination (6 x 2.24 Å)$_{PND}$ while O_{int} stands at its vertices (d(Yb-O_{int}) = 2.89 Å)$_{PND}$ similarly to the 6+1 coordination of yttrium in $YMnO_3$ (apical Y-O distance of <2.33-2.43 Å>).[3,4] However the FeO_5 parent TBP is strongly distorted due to the vicinity of O_{int}.

- One can derive from the MEM maps a general trend: for all atoms a huge increase of the spread of the MEM nuclear densities (drawn at the same spatial scale and same isosurface level on figure 6) is observed with regard to $YbFe_2O_{4.0}$. This effect is particularly pronounced for the anionic

sublattice. As explained above this general feature is at first sight the consequence of the presence of a strong positional modulation induced by the oxidation process, modulation viewed in "counter-relief" through this "average" structural description. Hence to conclude rather homogeneous modulated displacements are expected for O1, O2 and O_{int}, and to a lesser extent for Fe and Yb.

Table 3: atomic coordinates and displacement parameters for $YbFe_2O_{4.5}$ at RT from PND data (space group P-3, a=3.4675(3) Å, c=8.3748(8) Å, R_{Bragg} = 5.44 %)

Atom, site, occ	x	y	z	U_{iso} / U_{eq}	$U_{11}=U_{22}$	U_{33}	U_{12}	$U_{13}=U_{23}$
Yb, *1a*	0	0	0	0.040(4)	0.037(4)	0.047(4)	0.018(4)	0
Fe, *2d*	2/3	1/3	0.3452(8)	0.023(2)	0.0135(16)	0.043(2)	.0067(16)	0
O1, *2d*	2/3	1/3	0.118(1)	0.068(4)				
O2, *2d, 0.76(2)*	1/3	2/3	0.405(1)	0.037(3)				
O_{int}, *2c,0.49(2)*	0	0	0.347(2)	0.031(5)				

5.2 Identification of the Modulated phenomena:

Similarly to the ED study performed on $YbFe_2O_{4.0}$, one has to distinguish main structural modulations occurring in the oxidized form. The ED study of $YbFe_2O_{4.5}$ reveals two kinds of satellites of totally different origin. The first one is characterized by very weak intensities observed in the $[-110]_h$ ZAP (fig. 5a) corresponding to $q_{1.2,\ YbFe2O4.5}$ ~ 0.36 a_h^* + 0.36 b_h^*. To the best of our knowledge, this *in-plane* modulation was never reported in other $LnFe_2O_{4+x}$ phases. However, in analogy to all phenomena reported so far in the $[-110]_h$ ZAP they are assigned to CO domains. It could ideally be related to residual Fe^{2+}/Fe^{3+} ordering in non-stoichiometric minor domains with $YbFe^{\sim 3+}{}_2O_{4.5-x}$ nominal stoichiometry. The related diffraction features have not been observed neither on XRD nor PND patterns, and this modulation may be considered as non-representative of a long range structure.

The main satellites, indexed using the modulation vector $q_{1,\ YbFe2O45}$, as ~0.27 a_h^* + ~0.36 c_h^* appears in the [010] ZAP (fig. 5b) as well as in the [100] ZAP by three-fold axis twinning (q_{1T}) already described [12,13], see fig. 5c. They are of primary importance because also observed/refined in our PND data detailed in 5.3. $q_{1,\ YbFe2O45}$ is in accordance with the one reported for the Lu analog, i.e. $q_{1,LuFe2O5-x}$ = ~0.31 a_h^* + ~0.33 c_h^*. However during oxidation of $LuFe_2O_4$ into $LuFe_2O_{4.5}$ the evolution of the satellite spots, into a commensurate orthorhombic cell (called O), via a modulated monoclinic intermediate (called M') was mentioned.[13] We found no evidence of such commensurate-locking, nor any clues for a monoclinic symmetry in $YbFe_2O_{4.5}$, comforting our average refinement in the $P\bar{3}$ space group. The Figure 5d shows Yb undulations along c (periodically every ~ 3 Yb atoms) reminiscent of the stoichiometric case (fig. 3f). By analogy with the $YbFe_2O_{4.0}$ case, we already suggested in 5.1 its weak influence on the intensities of the modulated PND satellites due to short range correlations. Our ED patterns are homogeneous between all tested crystallites and samples, but sometimes show

the existence of diffuse streaks along c* on [010] ZAP. The corresponding HAADF image shows perturbation of the ideal AA stacking mode between two next Yb layers into a AB stacking (red arrows on the figure 5 f). These stacking faults are reminiscent of the parent $YbFe_2O_4$ structure and occasionally responsible for the peak asymmetry of the high resolution synchrotron XRD patterns.

5.3 Modelling the real $YbFe_2O_{4.5}$ structure by the superspace crystallographic approach:

The average structural description is genuinely limited as based only on the main diffracted peaks reflecting an idealized periodic order, neglecting the O2-O_{int} interplay and related atomic shifts. However, the $q_{1, YbFe2O4.5}$ structural modulation (not related to any CO phenomenon) was detected on synchrotron XRD and PND patterns, which allows for the first time to propose a real atomistic description of $RFe_2O_{4.5}$.

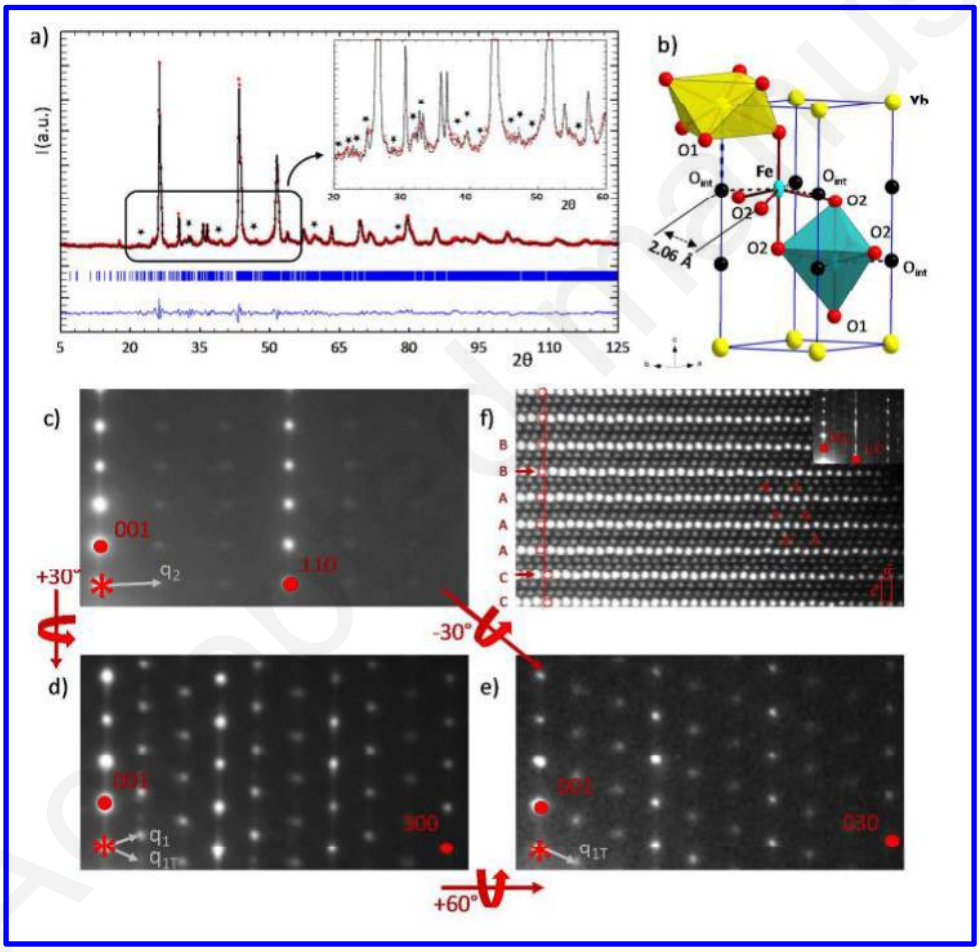

Figure 5: *PND Rietveld refinement of a) $YbFe_2O_{4.5}$* (* show main modulation satellites) *and the b) refined average crystal structure. Electron diffraction Zone axis patterns of $YbFe_2O_{4.5}$: c) [-110] with q_2 (CO) modulation vector. d) [010] e) [100] with q_1 and q_{1T} (structural) vectors f) HAADF image of d) with diffuse streaks along c*. Empty red arrows indicate an undulation of Yb every three atoms. Stacking faults (filled red arrows) concern the occasional AA stacking between next Yb layers.*

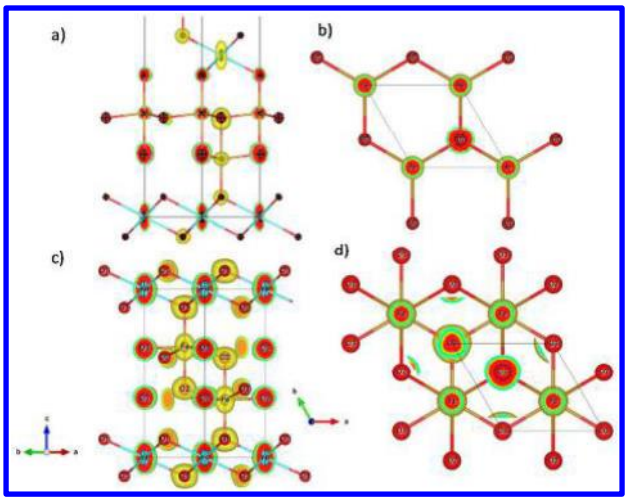

Figure 6: *Distribution and slices of nuclear densities obtained at RT for a,b) $YbFe_2O_{4.0}$ and c,d) $YbFe_2O_{4.5}$ by MEM from NPD data. O3 refers to interstitial O_{int} sites. Isosurface levels are set at 0.24 fm/Å^3. The structural model obtained by Rietveld refinement against PND data is also shown with atomic displacement ellipsoids drawn at the 50% probability level.*

The stacking faults mentioned in 5.2 play against extended modulated domains at least along the *c* axis. It results in broadened widths of the modulated satellites. The $q_{1,YbFe2O45}$ components were refined to 0.309(2), -0.029(2), $0.352(2)_{synchr.}$ using a secondary phase assorted with a broad profile, see fig. S3b. This broadening is less critical concerning the PND experimental resolution while their enhanced intensities denote an important oxygen contribution. The profile fitting shown figures S3c,d leads to the $q_{1,YbFe2O45}$ components : 0.278(1), -0.020(1), $0.359(2)_{PND}$ using 1st and 2nd order satellites. The incommensurate modulation vector (α,~0,γ) being inconsistent with any trigonal super-symmetry (from superspace tables) we reduced the 3D+1 symmetry to the most symmetrical subgroup compatible with P3, i.e. P-1(α,β,γ)0 which gives a consistent model. Although dealing with a triclinic superspace distortion, trigonal restraints have been applied to atomic coordinates and anisotropic thermal parameters such that only the modulated waves follow the triclinic relaxation. In general, for meaningful results, we have treated this case using:

- only 1st order displacive modulations for all atoms, after carefully checking that they improve the convergence of the least-squares fit. We note that best fits can be reached using 2nd order displacive waves but have been discarded.

- Modulated occupational characters of both O2 and O_{int} are modelled through Cresnel functions based on the observation of F_{obs} Fourier maps, i.e. empty or filled sites along the fourth-space i dimension, see figure 7a. It finally leads to *R*(all)= 3.87% *R*(main)= 2.60% , *R*(1st sat.)= 4.52% *R*(2nd sat.)= 4.61%, see Figure 5a and crystallographic/modulation parameters in S5. We note several striking points:

i) The displacive modulation along *z* (Å) for Yb, Fe and oxygen atoms are shown Figure 7b, c. It validates the rather significant d*z* amplitude of Fe and oxygen atoms predicted from the MEM results calculated using as constraints the fundamental (main peaks) intensities only.

ii) The conservation of short O2-O_{int} distances in some superspace areas play for imperfect ordering, due to domain boundaries. It follows that the stoichiometry restrictions (O2 + O_{int}) have been removed in the last cycles leading to the refined $YbFe_2O_{4.89}$ formula from which some oxygen should be removed when involved in short O-O contacts.

iii) Finally, the model generate reasonably well the observed satellites and the refined crystal structure is consistent apart of local superspace areas with too short Oint-O2, Yb-O1 and/or Fe-O distances, see the highlighted areas in Fig. 7d-f. Those minor discrepancies result from the miss-estimation of some satellites intensities, using a common profile function as for the main peaks while satellites are broader than the latter. Also, it is expected that the use of smooth 1st order displacive waves only generate approximations, but sounds more reasonable dealing with powder diffraction. Finally, the occurrence of local disorder mentioned above gives rise to an excess of oxygen anions in the 3D+1 refinement.

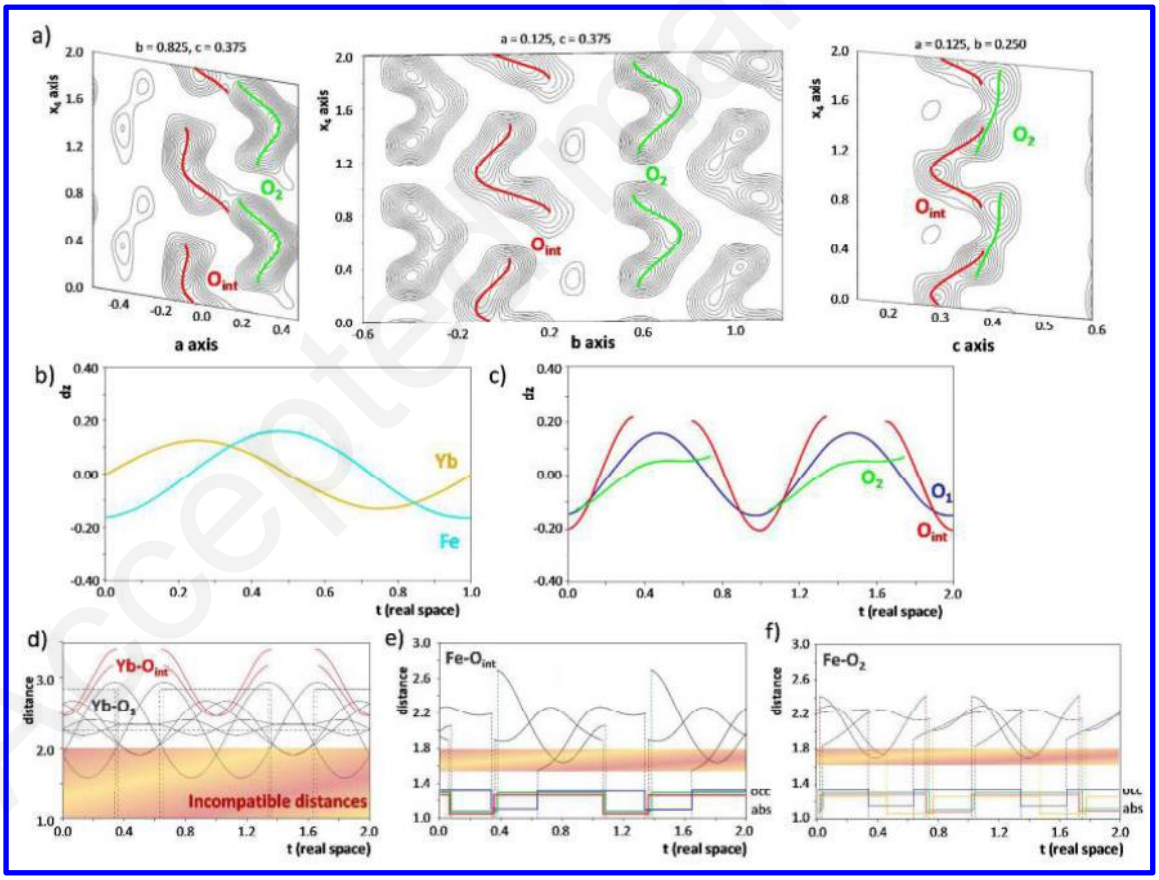

Figure 7: a) atomic strings for O2 and O_{int} superposed on the summed F_{obs} Fourier maps in the x4-x, x4-y, x4-z planes to integrate the full nuclear density (a axis: 0.55<b<1.1 and 0.3<c<0.45), (b axis: -0.15<a<0.4 and -0.3<c<0.45) and (c axis :-0.15<a<0.4 and 0.15<b<0.6). b, c) displacement along z (Å)

of all atoms against t (real space projection of the x4 axis). d-f) cation-anion distances along t with evidence of holes due to the Cresnel occupancy of O2 and O_{int}. A part of the strings should be excluded due to incompatible distances.

5.4 Real space model and FeO_n polyhedra: figure 8 highlights the modification of the $YbFe_2O_{4.0}$ structure (fig.8a,b) after oxygen uptake (fig.8 c-e). After projection of the refined superspace structure of $YbFe_2O_{4.5}$ in the real space using a periodic 18x3x2 cell approximation, we obtain the model shown figure 8e. The alternation of O_{int} and O2 in the 4^{th} dimension creates a complex sequence of individual (O2 or O_{int}) areas and mixed (O2 + O_{int}) ones in the 3D space. The modulation create undulations of the YbO_2 layers and Fe/O double layers, out-of phase across the layers due to the $q_{.1}$ component along c*, see Figure 8d. Within layers modulated rows of various polyhedra are observed along the *a*-axis while the polyhedral suite is nearly unchanged along *b* due to the negligible -0.017 b* component. The refined sinusoidal displacement waves push aside O2 and O_{int} rather efficiently although short O2-O_{int} distances remain. The figure 8e was built removing all O-O distances shorter than 2.2 Å. Distorted FeO_6 octahedra occur in the cell combining O2 and O_{int} while the absence of the apical O2 corner created FeO_5 square pyramids. In some cells the original TBPs are conserved, formed solely in-plane of three O2 or three O_{int} atoms. Here, strikingly in the cells with lack of the apical O2 corner we find FeO_4 tetrahedra unexpected dealing with O intercalation in a FeO_5 TBP matrix. The oxygen distribution between two layers of a double-layer respects the 4D centrosymmetric P-1(α,β,γ)0 super-space group which stabilizes a homogeneous segregation of oxygen anions.

The variety of interacting FeO_n polyhedra after oxidation was confirmed by Mössbauer spectroscopy shown Figure 3b and S3e. It can be reconstructed with three components associated with trivalent iron ions in four-, five- and six-fold coordinations (Table 2). Here again with respect to the experimental resolution (0.30 mm/s linewidth), the Fe^{3+}[5] and Fe^{3+}[6] signatures were calculated using a distribution of the quadrupole splitting parameter (Δ), where dealing with spherically symmetric electronic distribution in high spin d^5 Fe^{3+} ions, the quadrupole splitting arises mainly from the lattice contribution to the electric field gradient (EFG) through the crystal field. The distribution of the octahedral contribution is pronounced. However, we note that this fit was preferred to other unsatisfactory models (*e.g* Fe^{3+} [5] and Fe^{3+}[6] only) leading to broad sub-spectra characterized by hyperfine parameters (δ and Δ) which are clearly not consistent with the structural features. Within the modulated 3D-structure of $YbFe_2O_{4.5}$ (Figure 8), the aperiodic distribution of FeO_n polyhedra induce some heterogeneity in the Fe-O bond lengths for each iron site (especially for FeO_5 and FeO_6 polyhedra) and thus, slight variations of the EFG at the ^{57}Fe nucleus. This variability of distortion in iron sites is clearly reflected by the width and the multimodal character

of the observed Δ distributions especially for the six-fold coordinated Fe^{3+} ions (Figure3b). No Fe^{2+} Mössbauer signal was observed above the detection limits.

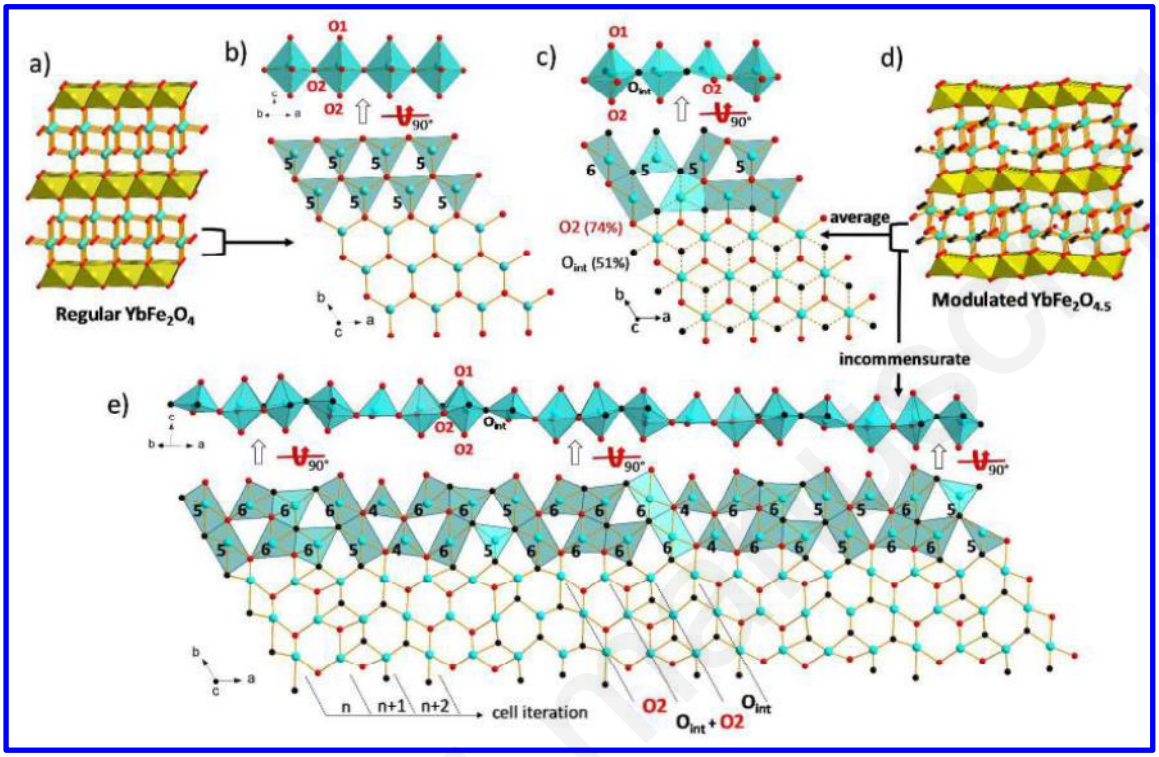

Figure 8: a,b) crystal structure of $YbFe_2O_{4.0}$ with detail of an equatorial plane in the bilayer and corresponding rows of TBPs along the a-axis. c) Equatorial plane from the average $YbFe_2O_{4.5}$ structure with interplay between O2 and O_{int} and a plausible row with several FeO_n coordinations. d) Undulations in the modulated 3D-structure of $YbFe_2O_{4.5}$ from the 3D+1 superspace treatment. e) It yields incommensurate distribution between O2 and O_{int} leaving complex rows with various FeO_n polyhedra, n=4,5,6. After removal of some oxygen, the shortest O-O distance to build the polyhedral is 2.2 Å, taking into account that the displacive atomic waves are not perfectly simulated.

6) Driving force of the structural rearrangement during redox cycles

The redox chemistry of iron in Fe^{3+}/Fe^{4+} systems is well known dealing with perovskite-based materials and generally retain stable mixed state progressively reduced on heating as abundantly described in the literature, see $SrFeO_x$ compounds [33] or more exotic hexagonal $BaFe(O,F)_x$ phases. [34] In the Fe^{2+}/Fe^{3+} case concerned here, the redox potential plays for stable trivalent iron compounds after annealing which uncontestably drives the $YbFe_2O_4$ oxidation at moderate temperature. However, it is worth identifying the key-structural parameters involved in the reconstructive process. Three distinct main structural routes are associated to the $Fe^{2+} \rightarrow Fe^{3+}$ oxidation in solid oxides:

- the filling of oxygen vacancies with "minor" reconstructive changes of the cationic sub-lattice sometimes in absence of any thermal activation, e.g. see the slow oxidation of magnetite Fe_3O_4 into

maghemite γ-Fe_2O_3 with conservation of the spinelle structure, and the spontaneous oxidation of $YBaFe^{+2.25}{}_4O_{7.0}$ into $YBaFe^{+2.5}{}_4O_{7.5}$ at room temperature and further oxidation on post-annealing.[35]

- the topochemical oxidation by exsolution of Fe_2O_3 starting from Fe^{2+} based oxo-anion compounds, e.g. $Fe_3(PO_4)_2 \rightarrow Fe_2(PO_4)_2$, [36] $LiFe(PO_4) \rightarrow LiFe_{1-x}(PO_4)$,[37] $BaFe_2(PO_4)_2$ ⇔ $BaFe_{1.33}(PO_4)_2$. [38,39]It involves long Fe diffusion paths generally activated around *ca.* 300°C in the case of iron phosphates.

- the restacking of the cation-based layers concerned in this work. This process is rare but was recently reported during the reversible reduction/re-oxidation of the layered $YMnO_{2.5}$ into $YMnO_3$ [4], see figure 9a,b. In this case, the change of coordination from tetrahedral Mn^{2+} to TBP Mn^{3+} is accompanied by a [BAB] to [CAB] restacking very similarly to the $YbFe_2O_4$ oxidation, see fig.9c,d. The analogy between these two examples highlight the particular role of the rare earth and particularly its apical R–O bonds which self-adapt to the concentration of oxygen in the upper layer, after shearing. The versatile rare earth coordination number between 6, 6+1 or 6+2 combined with the transition metal configurational change interact strongly such that the oxidation is processed at medium temperatures.

-

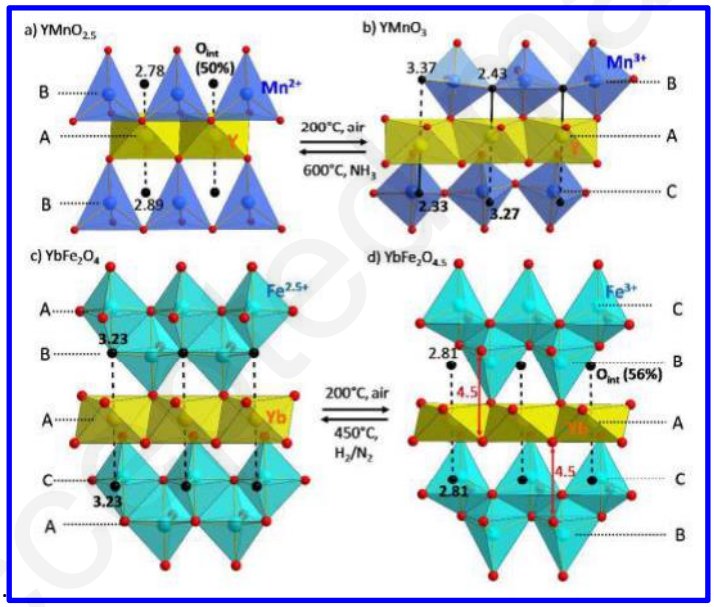

Figure 9 : restacking between the reversible oxidation/reduction of a,b) $YMnO_{2.5}$ into $YMnO_3$ c,d) $YbFe_2O_4$ into $YbFe_2O_{4.5}$ with evidence of apical R-O bonds driving the system.

7) Electronic properties upon oxidation

7.1 Evidence of a magnetically frozen state: Starting from the 3D-ferrimagnetic $YbFe_2O_4$ below 240

K [40,41] (see figure 10a. and supplementary S6 for details), the oxidation into $YbFe_2O_{4.5}$ has drastic effects on magnetic properties. The susceptibility measured for $YbFe_2O_{4.5}$ shows strong antiferromagnetic correlations with smooth deviation from the Curie-Weiss law below *ca.* 200 K. We found θ_{CW} = -239.6 K and an effective moment of √(8C) = 9.06 μB/Oe.FU (C=10.26) very close to the expected μ_{eff} =9.51μB/Oe.FU (C=11.32) calculated by summing the Curie contributions ($g^2(J(J+1)/8)$ for each atoms, i.e. two Fe^{3+} : g=2, J=S=5/2 and one Yb^{3+}: g =8/7, J =7/2. The ZFC/FC divergence and anomaly at 8 K is assigned to the spin reorientation of the $YbFeO_3$ minor second phase [42]. No antiferromagnetic ordering was observed on the PND patterns in good agreement with the distribution of FeO_n polyhedra and Fe-Fe exchanges. Only a broad peak appears at Q=1.25 $Å^{-1}$ growing below 200 K, fig.10b and S6. It corresponds to correlation pairs distance d= 2π x 1.23/Q = 6.1Å applying the Debye formula for diffuse scattering. This typical correlation distance corresponds to the Fe---Fe next-nearest neighbor distances inside the double layers (6.03 and 5.96 Å in plane and out-of-plane respectively), but should also involve the shortest Fe---Fe separation across the $[YbO_2]$ spacer (6.06 Å). Although difficult to distinguish, both in-layers and in-between-layers medium range magnetic correlations are expected in $YbFe_2O_{4.5}$ on the basis of the pristine ferromagnetic material. The 3D magnetic interplay was proved by ^{57}Fe Mössbauer spectroscopy performed at 4.2 K. In both $YbFe_2O_{4.0}$ and $YbFe_2O_{4.5}$ all iron ions are influenced by strong local magnetic fields in a "frozen" state. Indeed, the Mössbauer spectrum of $YbFe_2O_{4.5}$ recorded at 4.2 K (Figure S6f) exhibits three magnetic components, *i.e.* three sextets characterized by hyperfine magnetic fields ranging from 43 to 48 T, while the spectrum of the parent phase (see supplementary, Figure S6f) appears far more complex with at least three magnetically ordered components (two due to Fe^{3+} ions and another associated with Fe^{2+} ions) and a broad unresolved (not fully ordered) magnetic signal.

7.2 Towards localized transport: Concerning the electric transport, it was reported that $YbFe_2O_4$ presents a large non-linear resistive ρ(T) regime.[43] Typically the experimental resistivity increases on decreasing the applied current, while the divergence from linearity increases on cooling. Since such general behavior can occur in activated semiconducting conductors due to current induced sample self-heating, the genuine origin of this effect is still under debate. Most recent experiments in $YbFe_2O_4$ give some clues for an intrinsic non-linear process in this material, below the CO temperature due to the extension of ordered 3D Fe^{2+}/Fe^{3+} domains.[44] During our measurements, we observed that the first signs of non-linear resistivity at T≲320 K, i.e. very close to T_{CO} around 340 K (see fig.10c), while the strongest non-linear effects occurs at *ca.* 200 K, consistently with previous reports. [41] . After full oxidation, $YbFe_2O_{4.5}$ shows an insulating regime (ρ = *ca.* 10^6 -10^7Ω.cm at 350 K)

and rapidly reaches out-of-range values. It is assigned to the effect of the strongly localized electronic transport in a pseudo-periodic arrangement of single valent Fe^{3+} ions.

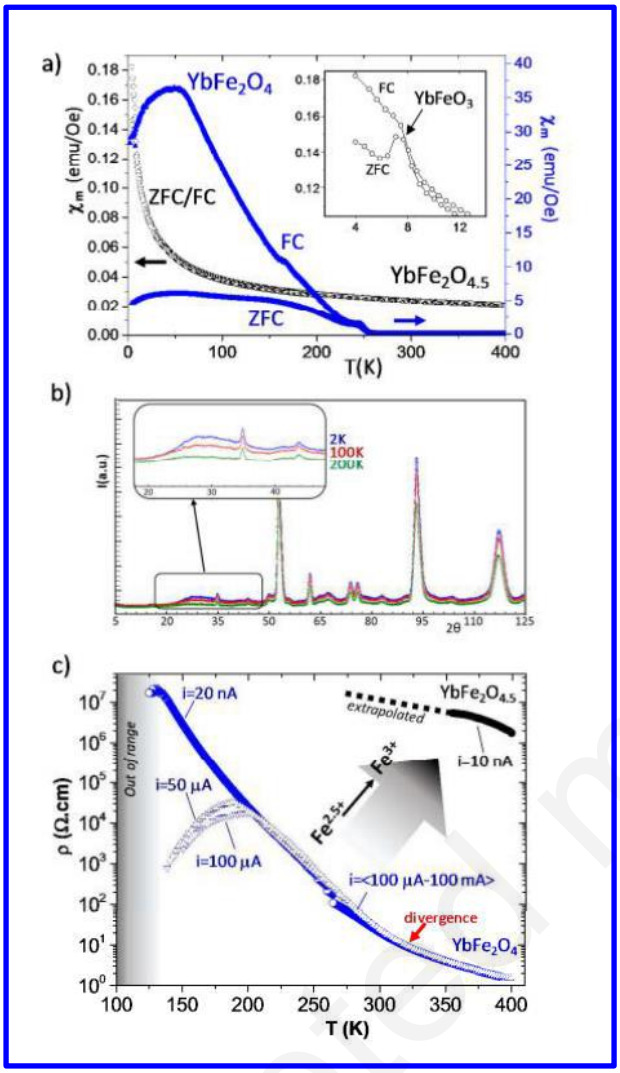

Figure 10: a) χ(T) for $YbFe_2O_4$ and $YbFe_2O_{4.5}$ with expected ZFC/FC divergence for the former [38,39] . The smooth temperature dependence for $O_{4.5}$ is only interrupted by the $YbFeO_3$ (2^{nd} phase) transitions, see inset. b) PND of $YbFe_2O_{4.5}$ on cooling with magnetic diffuse scattering growing. c) Electric transport before (non linear ρ(I) regime below 320K) and after (insulating regime) oxygen uptake.

8) Conclusion

In conclusion we have shown that the hyperstoichiometric $YbFe_2O_{4.5}$ material can be obtained by a reversible topotactic (according to the IUPAC nomenclature) oxidation of the pristine $YbFe_2O_4$ while retaining the layered character of the multiferroic ferrite. At the average structural level $_\infty[YbO_2]$ modules are conserved during the transformation but rearranged through the breakage of external Yb—O bonds, leading to a cooperative gliding

of the Yb and Fe layers along with a full reorganization of the anionic sublattice in the iron bilayers.

Beyond this average description, we have been able to unravel the real incommensurately modulated crystal structure of $YbFe_2O_{4.5}$ by the means of a crystallographic refinement within the superspace group approach against PND data. This analysis gives unique crystal chemistry insights rather unexpected in particular for the highly labile $_\infty[Fe_2O_{2+x}]$ blocks. The aperiodic occupational and positional modulations of their inner oxygen creates a unique distribution of FeO_4, FeO_5 and FeO_6 polyhedra. Such features definitely highlights the amazing structural flexibility of those triangular ferrite blocks. The aforementioned restacking between the modules is controlled by the aptitude of the Yb^{3+} ions to adopt more or less distorted YbO_6, YbO_{6+1} and YbO_{6+2} coordinations while the "intrinsic" structural undulations inside the $_\infty[YbO_2]$ modules (already present in the pristine compound) are drastically amplified during the oxidation process and plausibly assist the oxidation process which starts as low as 200°C. The reversible reduction in mild conditions suggests promising anionic transport and electrochemical properties highlighted by the OSC of 1434 µmol-O_2/g. It is noteworthy that by analogy with the $LuFe_2O_{4+x}$ case for which several intermediate oxidized forms have been detected by electron diffraction all along the oxidation, versatile Fe^{3+}/Fe^{2+} orderings should pave the way to RFe_2O_{4+x} with increasing dielectric properties against the iron mean oxidation state, as confirmed by the insulating $YbFe_2O_{4.5}$ character. Together with the extension of antiferromagnetic exchanges brought by increasing the Fe^{3+} high spin contributions, the controlled oxidation opens a broad field of future investigations searching for multiferroicity in those layered oxides owing to the redox/structural key-parameters demonstrated here.

Acknowledgements

This work was carried out under the framework of the Multi-InMaDe project supported by the ANR (Grant ANR ANR-16-CE08-0023). The Fonds Européen de Développement Régional (FEDER), CNRS, Région Nord Pas-de-Calais, and Ministère de l'Education Nationale,de l'Enseignement Supérieur et de la Recherche are acknowledged for funding the X-ray diffractometers. Chevreul Institute (FR 2638), Ministère de l'Enseignement Supérieur et de la Recherche, Région Nord – Pas de Calais and FEDER are acknowledged for supporting and

funding partially this work. We thank Katya Montcrieff , Laurence Burylo and Nora Djellal for help concerning the experimental job.

Supporting informations :

The supporting information is available free of charge on the ACS publication website at DOI **********. It includes essentially more detailed crystallographic informations and specific explanations. Further details of the crystal structures may be obtained from the Fachinformationszentrum Karlsruhe, 76344 Eggenstein-Leopoldshafen, Germany (Fax: +49-7247-808-666; e-mail: crysdata@fiz-karlsruhe.de, http://www.fiz-karlsruhe.de/request_for_deposited_data.html) on quoting the depository numbers CSD–433214, and CSD–433213 for the average and modulated models of $YbFe_2O_{4.5}$.

References

(1) Dong, S.; Liu, J.-M.; Cheong, S.-W. *Adv. Phys.* **2015**, *64*, 519–626.

(2) Isobe, M.; Kimizuka, N.; Iida, J.; Takekawa, S. *Acta Crystallogr. Sect. C* **1990**, *46*, 1917–1918.

(3) Overton, A. J.; Best, J. L.; Saratovsky, I.; Hayward, M. A. *Chem. Mater.* **2009**, *21*, 4940–4948.

(4) Kabbour, H.; Gauthier, G. H.; Tessier, F.; Huve, M.; Pussacq, T.; Roussel, P.; Hayward, M. A.; B, Z. L. M.; Marinova, M.; Colmont, M.; Colis, S.; Mentre, O. *Inorg. Chem.* **2017**, *56*, 8547–8553.

(5) Horibe, Y.; Ikeda, N.; Yoshii, K.; Mori, S. *Phys. Rev. B - Condens. Matter Mater. Phys.* **2010**, *82*, 1–5.

(6) Abughayada, C.; Dabrowski, B.; Avdeev, M.; Kolesnik, S.; Remsen, S.; Chmaissem, O. *J. Solid State Chem.* **2014**, *217*, 127–135.

(7) Bourgeois, J.; Hervieu, M.; Poienar, M.; Abakumov, A. M.; Elkaïm, E.; Sougrati, M. T.; Porcher, F.; Damay, F.; Rouquette, J.; Van Tendeloo, G.; Maignan, A.; Haines, J.; Martin, C. *Phys. Rev. B - Condens. Matter Mater. Phys.* **2012**, *85*, 1–10.

(8) Christianson, A. D.; Lumsden, M. D.; Angst, M.; Yamani, Z.; Tian, W.; Jin, R.; Payzant, E. A.; Nagler, S. E.; Sales, B. C.; Mandrus, D. *Phys. Rev. Lett.* **2008**, *100*, 2–5.

(9) Zhang, Y.; Yang, H. X.; Ma, C.; Tian, H. F.; Li, J. Q. *Phys. Rev. Lett.* **2007**, *98*, 2–5.

(10) Ikeda, N.; Ohsumi, H.; Ohwada, K.; Ishii, K.; Inami, T.; Kakurai, K.; Murakami, Y.; Yoshii, K.; Mori, S.; Horibe, Y.; Kitô, H. *Nature* **2005**, *436*, 1136–1138.

(11) Hervieu, M.; Damay, F.; Poienar, M.; Elkaïm, E.; Rouquette, J.; Abakumov, A. M.; Van Tendeloo, G.; Maignan, A.; Martin, C. *Solid State Sci.* **2013**, *23*, 26–34.

(12) Hervieu, M.; Damay, F.; Maignan, A.; Martin, C. *Solid State Sci.* **2015**, *48*, A1–A16.

(13) Hervieu, M.; Guesdon, A.; Bourgeois, J.; Elkaim, E.; Poienar, M.; Damay, F.; Rouquette, J.; Maignan, A.; Martin, C. *Nat Mater* **2014**, *13*, 74–80.

(14) Murakami, Y.; Abe, N.; Arima, T.; Shindo, D. *Phys. Rev. B* **2007**, *76*, 24109.

(15) Nagata, T.; Janolin, P.-E.; Fukunaga, M.; Roman, B.; Fujiwara, K. *Appl. Phys. Lett.* **2017**, *110*.

(16) McEvoy, A. J. *J. Mater. Sci.* **2001**, *6*, 1087–1091.

(17) A. Arico, P. Bruce, B. Scrosati, J. T. and W. V. S. *Nat. Mater.* **2005**, *4*, 366–377.

(18) Shao, Z.; Haile, S. M. *Nature* **2004**, *431*, 170–173.

(19) Petricek, V.; Dusek, M. ; Palatinus, L. Institute of Physics, Academy of Sciences, Praha, Czech Republic. 2006.

(20) Rodríguez-Carvajal, J. *Comm. Powder Diffr. (IUCr). Newsl.* **2001**, *26*, 12–19.

(21) Izumi, F.; Dilanian, R. A. In *Recent Research Developments in Physics, Vol. 3, Part II*; Transworld Research Network, Trivandrum, **2002**; pp 699–726.

(22) Fujio Izumi, K. M. *Solid State Phenom.* **2007**, *130*, 15–20.

(23) Brand, R. A.Winormos software, *Universität Duisburg*; **2008.**

(24) Hesse, J.; Rübartsch, A. *J. Phys. E.* **1974**, *7*, 526–532.

(25) Sun, F.; Wang, R.; Aku-Leh, C.; Yang, H. X.; He, R.; Zhao, J. *Sci. Rep.* **2014**, *4*, 6429.

(26) Tanaka, M.; Iwasaki, H.; Siratori, K.; Shindo, I. *Phys.Soc. Japan* **1989**, *58*, 1433.

(27) J.-C. Grenier, A. Wattiaux, A. Demourgues, M. P. and P. H. *Solid State Ionics* **1993**, *63–65*, 825–832.

(28) R. Gérardin, I. Nodari, H. Aqachmar, O. E. *Comptes Rendus des scéances l'Académie des Sci. Paris* **1982**, *295*, 863–865.

(29) Duffort, V.; Sarkar, T.; Serrao, C. R.; Pralong, V.; Caignaert, V.; Maignan, a.; Raveau, B. *J. Mater. Chem.* **2012**, *22*, 18923.

(30) Huang, X.; Ni, C.; Zhao, G.; Irvine, J. T. S. *J. Mater. Chem. A* **2015**, *3*, 12958–12964.

(31) Machida, M.; Kawamura, K.; Ito, K.; Ikeue, K. *Chem. Mater.* **2005**, *6*, 1487–1492.

(32) Sugiura, M. *Catal. Surv. from Asia* **2003**, *7*, 77–87.

(33) Takeda, Y.; Kanno, K.; Takada, T.; Yamamoto, O.; Takano, M.; Nakayama, N.; Bando, Y. *J. Solid State Chem.* **1986**, *63*, 237–249.

(34) Sturza, M.; Daviero-Minaud, S.; Kabbour, H.; Gardoll, O.; Mentré, O. *Chem. Mater.* **2010**, *22*, 6726–6735.

(35) Duffort, V.; Caignaert, V.; Pralong, V.; Barrier, N.; Raveau, B.; Avdeev, M.; Zheng, H.; Mitchell, J. F. *J. Solid State Chem.* **2012**, *191*, 225–231.

(36) Crouzet, C.; Recham, N.; Brunet, F.; Findling, N.; David, R.; Sougrati, M. T. *Solid State Sci.* **2016**, *62*, 29–33.

(37) Hamelet, S.; Gibot, P.; Casas-Cabanas, M.; Bonnin, D.; Grey, C. P.; Cabana, J.; Leriche, J.-B.; Rodriguez-Carvajal, J.; Courty, M.; Levasseur, S.; Carlach, P.; Van Thournout, M.; Tarascon, J.-M.; Masquelier, C. *J. Mater. Chem.* **2009**, *19*, 3979.

(38) Alcover, I. B.; David, R.; Daviero-Minaud, S.; Filimonov, D.; Huvé, M.; Roussel, P.; Kabbour, H.; Mentré, O. *Cryst. Growth Des.* **2015**, *15*, 4237–4247.

(39) David, R.; Kabbour, H.; Filimonov, D.; Huvé, M.; Pautrat, A.; Mentré, O. *Angew. Chemie - Int.*

Ed. **2014**, *53*, 13365–13370.

(40) Sun, Y.; Liu, Y.; Ye, F.; Chi, S.; Ren, Y.; Zou, T.; Wang, F.; Yan, L. *J. Appl. Phys.* **2012**, *111*, 07D902-07D902-3.

(41) Yoshii, K.; Mizumaki, M.; Matsumoto, K.; Mori, S.; Endo, N.; Saitoh, H.; Matsumura, D.; Kambe, T.; Ikeda, N. *J. Phys. Conf. Ser.* **2013**, *428*, 12032.

(42) Bazaliy, Y. B.; Tsymbal, L. T.; Kakazei, G. N.; Kamenev, V. I.; Wigen, P. E. *Phys. Rev. B - Condens. Matter Mater. Phys.* **2005**, *72*, 3–6.

(43) F. M. Vitucci, A. Nucara, C. Mirri, D. Nicoletti, M. Ortolani, U. Schade, and P. C. *Phys. Rev. B* **2011**, *84*, 153105.

(44) Nagata, T.; Fukada, Y.; Kawai, M.; Kano, J.; Kambe, T.; Dudzik, E.; Feyerherm, R.; Janolin, P. E.; Kiat, J. M.; Ikeda, N. *Ferroelectrics* **2013**, *442*, 45–49.

Table of content (for publication only)